Tau, G., et al., 2021, Shutting down dust emission during the middle Holocene drought in the Sonoran Desert, Arizona, USA: Geology, v. 49, https://doi.org/10.1130/G48550.1

Data Repository for

Shutting down dust emission during the middle Holocene drought in the Sonoran Desert, Arizona

Guy Tau[1,2*], Onn Crouvi[2], Yehouda Enzel[1], Nadya Teutsch[2], Paul Ginoux[3], and Craig Rasmussen[4]

[1] *Institute of Earth Sciences, Hebrew University of Jerusalem, Jerusalem 9190401, Israel.*

[2] *Geological Survey of Israel, 32 Yeshayahu Leibowitz, Jerusalem 9692100, Israel.*

[3] *National Ocean and Atmospheric Administration, Geophysical Fluid Dynamics Laboratory, Princeton, NJ 08540, USA.*

[4] *Department of Environmental Science, University of Arizona, Tucson, AZ 85721, USA.*

1. Methods

Current dust transport pathways and sources

Current dust transport pathways in the Sonoran Desert (SD), Arizona were analyzed using the National Oceanic and Atmospheric Administration (NOAA) Hybrid Single Particle Lagrangian Integrated Trajectory (HYSPLIT) model-4 (Draxler and Hess, 1998). The calculations were applied to 17 dusty days in the study area, based on the global data assimilation system (GDAS) archive, a global model with a 1˚ latitude-longitude grid. Air parcel backward trajectories were computed at the model ground level from Montezuma Well (MW) for 24-h before each dust storm. The selection of dates for analyses was based on two different databases: (1) The NOAA storm event data-base of Maricopa county in Arizona that includes ground-based observation of dust storms and (2) PM-10 data from the IMPROVE network via the United States Environmental Protection Agency Air Quality System (EPA-AQS) website, which measures aerosol concentrations and visibility. We examined the period from January 2011 to December 2019 and chose all days that exhibited above average PM-10 concentrations in Ikes Backbone, located 35 km south of MW. The IMPROVE network samplers collect 24-hour samples, every three days, and calculates the total dust

concentrations. Due to low temporal sampling resolution, short-lived dust storms can be masked. Thus, we chose days with PM-10 values higher than 30 µg/m^3 for summer and 20 µg/m^3 for winter. These values fit PM-10 values recorded from the IMPROVE network on known dusty days from NOAA storm event database. Moreover, selected dusty days air parcel trajectory's fits monitored modern dust movement from the SD (e.g. Breed and Reheis, 1999).

Current active dust sources in Arizona were identified using MODIS deep blue aerosol global data, based on a decadal high-resolution scale grid, as described by Ginoux et al. (2010). These data contain location of dust emission for different time scales (mostly in a day to a week). Hotspots were classified based on overlapped dust emission at the same geographical region throughout the dataset. The collocation of these hotspots with geomorphologic characteristics of preferential dust sources over the Chihuahuan desert has shown the potentiality of MODIS aerosol data to accurately detect dust sources (Baddock et al., 2016).

Active dust sources that were chosen for subsequent field sampling were only those that are located along current dust transport pathways observed in this study. All these dust sources were visited in the field, photographed, described, and surficial sediments (0 – 2 cm) of main geomorphic units in each source were sampled for laboratory analyses. Dust sources with high surficial coverage of vegetation and gravel, and/or that are characterized by medium to coarse sand texture (PSD mode coarser than 200 µm) were assumed as irrelevant for supplying dust to MW and therefore were not included in this paper.

Radiocarbon results and treatment

Age control was applied by combining the previous six ^{14}C ages reported by Davis & Shafer (1992) with eight ^{14}C samples that were analyzed in this study (Table S2). All previous samples (Davis & Shafer) were prepared and dated at the University of Arizona radiocarbon lab by AMS, except one sample dated by beta counting. New radiocarbon samples include charcoal/wood, Scrips seeds, large twig, twigs in varying sizes (as one sample) and insect wing. New samples were treated with acid-base-acid (1M HCl and 1M NaOH, 75°C) prior to combustion. The samples were dated by AMS at the radiocarbon lab of the University of California, Irvine. Three new samples were rejected due to reversal ages. All rejected samples are twigs of varying sizes that were hand-picked from the same depth. Because the variety in size and shape it is probable

that small ancient twigs participate and accumulated in the MW leading to a reversal age. Age-depth model was processed using Bacon, a Bayesian statistics analysis age-depth modelling package in R software (Blaauw and Christeny, 2011), that uses the IntCall3 calibration curve (Reimer et al., 2013).

Sampling the Montezuma Well core

The MW core is stored in a refrigerated storage of the University of Arizona in Tucson, Arizona. The core was described, photographed and a new core stratigraphy was composed. Snails and clams are the major characteristics of the upper section (0 – 550 cm; <9.3 ka), whereas uniform black mud with roots dominates the lower section of the core. Angular white carbonate rock fragments (1 – 5 cm) appear throughout the core. Twigs of various sizes and shapes characterize the depth interval of 430 – 500 cm (7.6 – 9 ka). We did not observe any evidences of debris-flow during our core description. We sampled with a total of 82 sub-samples that were collected with 5 ml plastic containers at an average interval of 12 cm and have been stored in the soil lab at the Geological Survey of Israel.

Adjacent soils and local bedrock sampling

Two soil profiles located approximately one km north from MW (34.65 N and 111.75 W; Fig. S1) were sampled. Three soil samples were taken for each: top-soil (0 – 0.5 cm), b horizon (0.5 – 3 cm) and c horizon (3 – 6 cm) for soil-1, and top-soil (0 – 3 cm), b horizon (3 – 8 cm) and c horizon (8 – 12 cm) for soil-2. Moreover, the soils are patchy, and cover about 50% of the surface. Few (10% vol.) weathered bedrock carbonate clasts (1 – 5 cm) are evident in the soil profile, mainly in the lower part. In addition, three rock fragments of the local MW bedrock and four samples from an escarpment near the soil profile were collected, all of Verde Formation.

Chemical composition analyses

Samples were crushed using a ball mill (Pulverisette 2, FRITSCH, Germany) after samples went splitting protocol and <2mm sieving. Powdered samples were fully dissolved by sodium peroxide (Na_2O_2) fusion (Brenner et al., 1980; Yu et al., 2001). Samples were prepared for major elements concentrations measurement by dilution (1:10,000) and additional Sc spiking as internal standard (final concentration of 5 mg/l) and measured by Inductively Coupled Plasma Optical Emission Spectrometry (ICP-OES, Optima 5300, Perkin Elmer, USA). Calibration was performed using commercial

elemental solutions. Four certified reference materials (CRMs; SO-1, SO-3, JLK-1, CCH) were processed and analyzed alongside the samples for determining and improving accuracy as well as 3 procedural blanks. Precision, accuracy, limit of detection (LOD) and procedural blank determinations are based upon four analysis sessions performed on different days and the results are shown in table S3. Precision was monitored by using two project standards resembling the MW core and Arizona's dust sources that were analyzed 15 times. Average precision value of Al, Fe and Ca is 2% and all better than 4%, 5% and 3%, respectively. Accuracy was determined on the four CRMs, as each CRM was analyzed 15 times. Accuracy average values of Al, Fe and Ca are 1%, 2% and 3%, respectively, and all better than 4% for Al and Fe, while Ca is better than 7%. The instrumental LOD was calculated on calibration blank analyzed 31 times throughout the four analytical session, yielding values of 0.08, 0.01 and 0.07 mg/l for Al, Fe and Ca, respectively. Procedural blanks included the entire sample processing protocol. The Al procedural blanks were found to be lower than the instrumental LOD, equivalent to <0.08 wt.% sample content. The Fe and Ca procedural blanks were determined as 0.01 and 0.7 wt.%, respectively.

Summer and winter chemical scores were calculated using the Al-Ca-Fe ternary diagram by projecting MW core samples towards a calculated summer or winter slope. The slope was calculated using linear regression over the entire summer or winter data points (without sub-categorizing such as alluvial fan, wash, etc.) that was forced to intercept at the origin axes (concentration of local bedrock). For each sample we calculated the projected relative distance between the summer and winter slopes. Thus, the relative ratio between summer and winter slopes was translated to their chemical score (in %). Core samples with relative Ca ratio (in the Al-Ca-Fe ternary diagram) higher than 90% were neglected as these represent mainly a bedrock source with negligible contribution of dust.

Particle size distribution (PSD)

Pretreatment of MW core samples, following Crouvi et al (2008) and Arcusa et al (2019) included: <2 mm sieving; sample splitting to 0.6 g aliquot, dissolving organic matter by shaking samples for 8 days with 20 mL of 10% NaOCl solution; calcium-carbonate removal with 25 mL 1M HCl shaken for 15 minutes; dissolving biogenic silica using 40 mL 10% Na_2CO_3 for 5 hours in a drying oven at 80 ° C; heavy fluid (S.G = 1.8) separation; <125 µm sieving; dispersion using sodium hexametaphosphate

solution, stirring for 5 minutes and ultrasonication for 30 seconds. Soil samples were treated with <2mm sieving; sample splitting to 0.6 g, calcium-carbonate removal with 25 mL 1M HCl shaken for 15 minutes. Samples from dust sources were analyzed as bulk. All samples were analyzed using Malvern Mastersizer MS-2000 laser diffraction device that measures PSD over the range of 0.02-2000 µm. Two to six replicate samples were subjected to three consecutive five seconds runs at a pump speed of 1800 RPM. The laser diffraction raw values were transformed into PSD using the Mie scattering model, with optical parameters of RI=1.52 and A=0.1. The soils mass of the > 2mm fraction of each sample was noted as well (Table S5).

End member modeling analysis (EMMA)

The EMMA approach considers compositional data constraints and provides sedimentological interpretable grain-size end members (EM); interpreted as proxies of sediment transport processes (Weltje, 1997; Weltje and Prins, 2003; Dietze et al., 2012). We used AnalySize MATLAB GUI package (Paterson and Heslop, 2015), designed specifically for unmixing PSD using least square measure for model quality and a non-negative matrix factorisation to estimate the EM distributions and abundance. Each indivdiual EM value is calculated in (%) via the AnalySize package, and their results are presented in Fig 4 (Summer EM is the value, in %, of both EM 2 and 3).

Calculated dust and bedrock fluxes of MW core

Total dust flux was calculated using Al content of each sample, divided by the average Al of the local bedrock (equation 1). The equation considers the accumulation rate (AR), and bulk density (ρ). Dust flux of individual EM was calculated by multiplying the total dust flux by the EM score.

$$\text{Dust Flux}\left[\frac{\text{g}}{\text{cm}^2\cdot\text{year}}\right] = \frac{\text{Al}_{\text{sample}}}{\overline{\text{Al}}_{\text{local bedrock}}}\cdot\text{AR}\left[\frac{\text{cm}}{\text{year}}\right]\cdot\rho_{\text{sample}}\left[\frac{\text{g}}{\text{cm}^3}\right]. \quad (1)$$

Bedrock flux was calculated using Ca content of each sample (equation 2), divided by the average Ca of dust sources, assuming that most Ca originates from the local bedrock collapsed into the well:

$$\text{Bedrock Flux}\left[\frac{\text{g}}{\text{cm}^2\cdot\text{year}}\right] = \frac{\text{Ca}_{\text{sample}}}{\overline{\text{Ca}}_{\text{Dust sources}}}\cdot\text{AR}\left[\frac{\text{cm}}{\text{year}}\right]\cdot\rho_{\text{sample}}\left[\frac{\text{g}}{\text{cm}^3}\right]. \quad (2)$$

A common practice for calculating dust flux includes dividing the dust immobile elemental proxy by the upper continental crust (UCC) value (equation 3) (Longman et

al., 2017; Pratte et al., 2017). Here, we divided the Al values of the samples by the local bedrock (depleted in Al), as it is obvious that the local carbonate is another potential source to the MW sediments. Hence, there is no benefit using the UCC values for MW. Due to low values of Al in the local bedrock (0.45 wt.%) compared to the UCC (8.2 wt.%), MW dust fluxes are relatively high compared to other calculated dust fluxes from the SW USA (Arcusa et al., 2019).

$$\text{Dust Flux}\left[\frac{\text{g}}{\text{m}^2\cdot\text{year}}\right] = \frac{\text{Al}_{\text{sample}}}{\bar{\text{Al}}_{\text{UCC}}}\cdot\text{AR}\left[\frac{\text{cm}}{\text{year}}\right]\cdot\rho_{\text{sample}}\left[\frac{\text{g}}{\text{cm}^3}\right]\cdot 10{,}000\left[\frac{\text{cm}^2}{\text{m}^2}\right]. \quad (3)$$

Raw results and proxies

The results of the MW core properties (depth, age, elemental composition, dust and bedrock flux, PSD, texture and scores) are shown in table S4; bedrock and soils properties (location, depth, PSD, texture and elemental composition) in table S5, and the dust sources properties (sampling location, vegetation and gravel cover, PSD, texture and chemical composition) in table S6 and S7. For the different calculated core proxies (Dust flux, fine and coarse dust fluxes, winter and summer scores) results were plotted as moving average using 3 data points for the entire data (Fig. 4).

2. Tables and figures

Table S1. Selected 17 modern dusty days classified by climate system and source of database.

Date	Data Reference	Date	Data Reference
Summer		Winter	
05-Jul-11	Known Haboob	**09-Feb-12**	Improve
18-Aug-11	Improve	**07-Mar-12**	Improve
17-Jun-12	Improve	**16-Apr-15**	Improve
21-Jul-12	NOAA Data Base	**07-Mar-16**	Improve
12-Jul-13	NOAA Data Base	**23-Mar-16**	Improve
13-Jul-14	NOAA Data Base	**08-Arp-18**	Improve
05-Aug-16	Improve		
21-Aug-16	NOAA Data Base		
08-Aug-18	NOAA Data Base		
22-Jul-19	NOAA Data Base		
23-Sep-19	NOAA Data Base		

Table S2. Radiocarbon samples from MW core

Current study

Sample Name	Depth [cm]	Material	Radiocarbon Age [yr. B.P]	δ13 C (%)	δ14 C (%.)	2σ Calibrated Age [yr. B.P]
GT-100	155	Twig	1290 ± 20	-	-148.2	1283-1224
GT-100	155	Charcoal	1410 ± 15	-	-160.7	1339-1293
GT-100	155	Scirpus seed	1260 ± 20	-	-145.3	1273-1175
GT-118**	620	Twigs	30,500 ± 310	-	-977.6	33,076-31,985
GT-121	757	Insect wing	9780 ± 170	-	-704.2	11,811-10,665
GT-121**	757	Twigs	29,190 ± 170	-	-973.6	31,841-31,011
GT-121	757	Charcoal	9490 ± 35	-	-693.1	10,814-10,651
GT-126**	942	Twigs	31,930 ± 320	-	-981.2	34,531-33,145

Davis and Shafer (1992) samples

Sample Name	Depth [cm]	Material	Radiocarbon Age [yr. B.P]	δ13 C (%)	δ14 C (%.)	Calibrated Age [yr. B.P]
AA-2450	220-230	Charcoal, wood	1526 ± 50	-	-	1527-1327
AA-2451	325-335	Charcoal, wood	2885 ± 60	-	-	3211-2867
AA-4693	390-400	Charcoal, wood	5540 ± 60	-	-	6470-6266
AA-2452	460-470	Scirpus achenes	8003 ± 70	-	-	9013-8649
A-4732**	530-540	"bark"	14,950 +350 – 320	-26.7	-	-
A-4733	887	Wood	9520 ± 200	-25.3	-	10,420
AA-5053**	887	Wood	24,910 ± 370	-	-	-
AA-4694	1015	Juniper twig	10,975 ± 95	-	-	12,225

****Rejected Samples**

Table S3. Major elements analytical parameters

	Al	Fe	Ca
Precision [%]	4	5	3
Accuracy [%]	4	4	7
LOD [mg/l]	0.08	0.01	0.03
Procedural Blank [wt.%]	< 0.08	0.01	0.07

Figure S1. A. Aerial photo (via Google Earth) of soil sampling location on a hilltop adjacent to MW. B. Field photo displaying the soils surface. C. Field photo of soil-2 profile (12 cm), revealing silty clay loam texture.

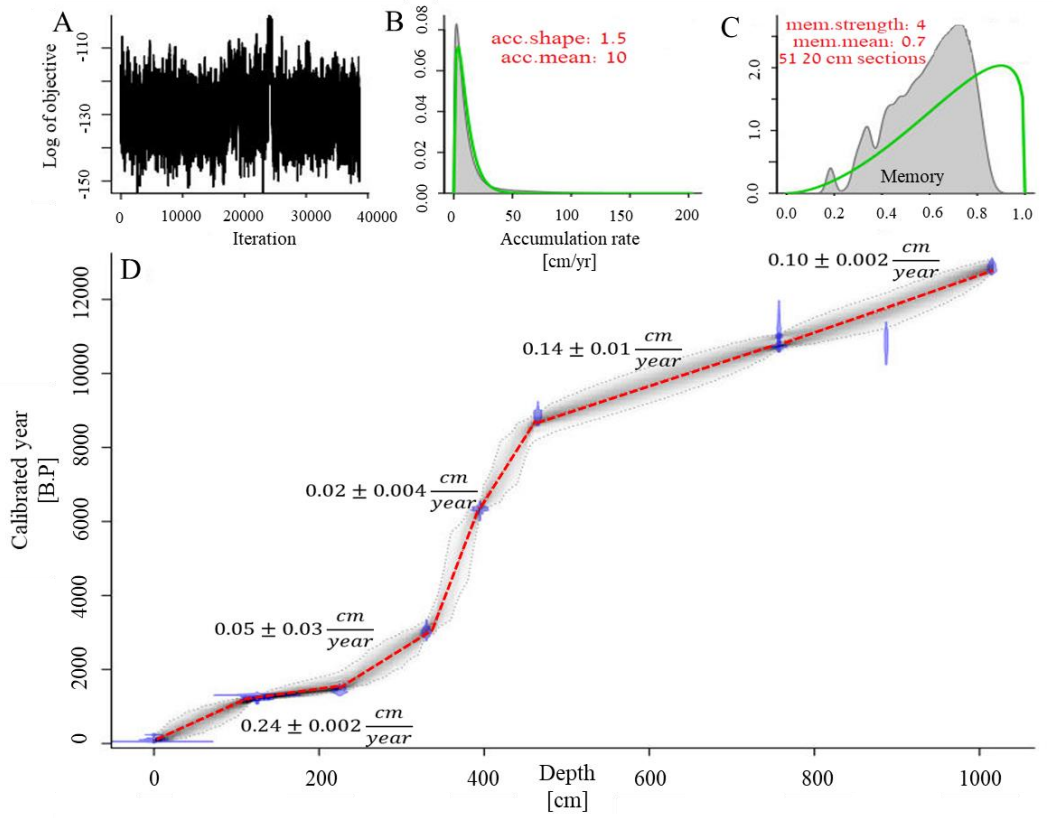

Figure S2. The MW core age–depth model via Bacon software. A. Graph indicates Markov chain Monte Carlo iterations. B, C. prior (green line) and posterior (grey histogram) distributions for the accumulation rate (B) and memory (C). D. Calibrated radiocarbon ages are in blue. Red line specifies the best age-depth model and grey dotted lines show 95% confidence intervals.

Table S4. The MW core properties (MA-moving average)

Sample	Depth	Calibrated Age	Accumulation Rate	Density	Mode	Texture	Al	Fe	Ca	MA-Winter PSD Score	MA-Summer PSD Score	MA-Winter Chemistry Score	MA-Summer Chemistry Score	Bedrock Flux	Dust Flux	MA-Dust Flux	MA-Fine Dust Flux
	cm	[ka B.P]	[cm/yr]	[g/cm^3]	[μm]	-	[wt. %]	[wt. %]	[wt. %]	[%]	[%]	[%]	[%]	[g/cm^2/yr]	[g/cm^2/yr]	[g/cm^2/yr]	[g/cm^2/yr]
MZW -411	130	1.3	0.24	0.3	56	Silt Loam	1.7	0.9	2.7	11	89	52	48	0.1	0.3	0.2	0.02
GT-01	139	1.3	0.29	0.3	n/a	n/a	1.9	0.7	1.8	n/a	n/a	29	71	0.05	0.4	0.4	n/a
MZW -412	146	1.3	0.29	0.3	46	Silt Loam	1.8	0.7	1.9	10	90	22	78	0.1	0.4	0.4	0.04
GT-100	155	1.3	0.30	n/a	64	Silt Loam	n/a	n/a	n/a	7	93	n/a	n/a	n/a	n/a	0.4	0.03
GT-02	163	1.4	0.29	0.3	n/a	n/a	1.9	0.8	5.4	n/a	n/a	10	90	0.1	0.3	0.4	n/a
MZW -413	170	1.4	0.29	0.3	n/a	n/a	1.7	0.6	5.4	n/a	n/a	11	89	0.1	0.3	0.3	n/a
GT-03	176	1.4	0.33	0.3	n/a	n/a	1.9	0.7	7.7	n/a	n/a	9	91	0.2	0.4	0.4	n/a
GT-101	178	1.4	0.29	n/a	66	Silt Loam	n/a	n/a	n/a	11	89	n/a	n/a	n/a	n/a	0.4	0.04
MZW -414	186	1.4	0.30	0.3	38	Silt Loam	1.8	0.70	11	8	92	7	93	0.3	0.4	0.4	0.03
GT-102	201	1.5	0.29	n/a	43	Silt Loam	n/a	n/a	n/a	8	92	n/a	n/a	n/a	n/a	0.4	0.03
GT-04	218	1.6	0.15	0.3	n/a	n/a	0.8	0.5	23	n/a	n/a	n/a	n/a	0.3	0.1	0.2	n/a
MZW -415	226	1.6	0.11	0.3	n/a	n/a	1.7	0.9	16	n/a	n/a	27	73	0.1	0.1	0.10	n/a
MZW -416	245	1.8	0.07	0.2	34	Silt Loam	1.0	0.6	31	15	85	n/a	n/a	0.2	0.04	0.08	0.01
GT-05	253	1.9	0.07	0.2	n/a	n/a	0.6	0.4	15	n/a	n/a	n/a	n/a	0.1	0.02	0.06	n/a
GT-06	261	2.0	0.07	0.4	n/a	n/a	1.3	0.6	19	n/a	n/a	n/a	n/a	0.2	0.1	0.05	n/a
GT-07	284	2.3	0.07	0.6	n/a	n/a	0.9	0.5	29	n/a	n/a	n/a	n/a	0.4	0.1	0.09	n/a
MZW -418	291	2.4	0.07	0.6	33	Silt Loam	1.3	0.6	23	23	77	n/a	n/a	0.3	0.1	0.1	0.02
GT-08	315	2.8	0.05	0.3	n/a	n/a	1.3	0.6	20	n/a	n/a	n/a	n/a	0.1	0.05	0.09	n/a
MZW -419	325	3.0	0.04	0.5	45	Silt Loam	1.5	0.6	18	28	72	27	73	0.1	0.1	0.08	0.02
GT-09	339	3.3	0.02	0.7	n/a	n/a	0.9	0.5	28	n/a	n/a	n/a	n/a	0.1	0.03	0.05	n/a
GT-103	343	3.5	0.02	0.6	27	Silt	0.7	0.4	31	14	86	n/a	n/a	0.1	0.02	0.04	0.01
GT-10	353	4.0	0.02	0.1	n/a	n/a	0.6	0.6	10	n/a	n/a	n/a	n/a	0.01	0.004	0.02	n/a
MZW -420	358	4.3	0.02	0.2	47	Silt Loam	0.7	0.5	16	13	87	n/a	n/a	0.02	0.01	0.008	0.001
GT-104	368	4.9	0.02	0.3	26	Silt	1.1	0.7	27	12	88	n/a	n/a	0.04	0.01	0.008	0.001
GT-11	376	5.3	0.02	0.4	n/a	n/a	3.1	1.3	10	n/a	n/a	35	65	0.02	0.1	0.02	n/a
MZW -421	384	5.8	0.02	0.5	34	Silt Loam	2.5	1.0	15	22	78	n/a	n/a	0.04	0.1	0.04	0.009
GT-105	388	6.0	0.02	0.5	43	Silt Loam	1.7	0.8	6.6	21	79	26	74	0.02	0.05	0.05	0.01
MZW -422	410	6.9	0.03	0.8	59	Silt Loam	2.6	0.9	15	20	80	31	69	0.1	0.1	0.08	0.02
GT-12	412	7.0	0.03	0.8	n/a	n/a	1.0	0.5	29	n/a	n/a	n/a	n/a	0.2	0.1	0.08	n/a
GT-106	415	7.1	0.03	0.7	41	Silt Loam	1.3	0.6	28	22	78	n/a	n/a	0.2	0.1	0.08	0.02
GT-107	429	7.6	0.03	0.5	25	Silt Loam	1.1	0.8	12	29	71	46	54	0.1	0.04	0.05	0.01
MZW -423	440	7.9	0.03	0.4	23	Silt Loam	n/a	n/a	n/a	40	60	48	52	n/a	n/a	0.05	0.02
GT-13	443	8.0	0.03	0.3	n/a	n/a	1.8	1.0	12	n/a	n/a	67	33	0.03	0.04	0.04	n/a
GT-108	450	8.3	0.05	0.3	28	Silt Loam	0.8	0.4	20	39	61	n/a	n/a	0.1	0.03	0.03	0.01
MZW -424	472	8.7	0.11	0.3	28	Silt	1.2	0.6	22	32	68	n/a	n/a	0.2	0.1	0.05	0.02
GT-109	481	8.8	0.14	n/a	36	Silt Loam	n/a	n/a	n/a	33	67	n/a	n/a	n/a	n/a	0.06	0.02
GT-14	490	8.9	0.14	0.3	n/a	n/a	1.0	0.6	12	n/a	n/a	67	33	0.1	0.1	0.08	n/a
MZW -425	497	8.9	0.14	0.3	39	Silt Loam	0.7	0.4	20	25	75	n/a	n/a	0.2	0.1	0.07	0.02
GT-110	504	9.0	0.14	n/a	32	Silt Loam	n/a	n/a	n/a	27	73	n/a	n/a	n/a	n/a	0.07	0.02
GT-15	508	9.0	0.14	0.3	n/a	n/a	1.2	0.5	12	n/a	n/a	53	47	0.1	0.1	0.09	n/a
GT-111	515	9.1	0.14	n/a	19	Silt Loam	n/a	n/a	n/a	32	68	n/a	n/a	n/a	n/a	0.1	0.03

Sample	Depth	Calibrated Age	Accumulation Rate	Density	Mode	Texture	Al	Fe	Ca	MA-Winter PSD Score	MA-Summer PSD Score	MA-Winter Chemistry Score	MA-Summer Chemistry Score	Bedrock Flux	Dust Flux	MA-Dust Flux	MA-Fine Dust Flux
	cm	[ka B.P]	[cm/yr]	[g/cm^3]	[µm]	-	[wt. %]	[wt. %]	[wt. %]	[%]	[%]	[%]	[%]	[g/cm^2/yr]	[g/cm^2/yr]	[g/cm^2/yr]	[g/cm^2/yr]
MZW -426	526	9.2	0.14	0.4	11	Silt Loam	3.0	1.3	2.0	58	42	36	64	0.03	0.3	0.2	0.1
GT-16	534	9.2	0.14	0.4	n/a	n/a	1.6	1.0	16	n/a	n/a	36	64	0.3	0.2	0.3	n/a
GT-112	540	9.3	0.14	n/a	43	Silt Loam	n/a	n/a	n/a	53	47	n/a	n/a	n/a	n/a	0.3	0.1
GT-113	555	9.4	0.14	n/a	40	Silt Loam	n/a	n/a	n/a	43	57	n/a	n/a	n/a	n/a	0.2	0.1
GT-17	556	9.4	0.14	0.5	n/a	n/a	1.0	1.3	20	n/a	n/a	n/a	n/a	0.4	0.1	0.1	n/a
MZW -427	562	9.4	0.14	0.4	28	Silt Loam	2.1	1.1	18	20	80	56	44	0.3	0.3	0.2	0.04
GT-114	571	9.5	0.14	n/a	41	Silt Loam	n/a	n/a	n/a	29	71	n/a	n/a	n/a	n/a	0.2	0.1
GT-18	578	9.5	0.14	0.4	n/a	n/a	0.9	0.7	14	n/a	n/a	n/a	n/a	0.2	0.1	0.2	n/a
GT-115	583	9.6	0.14	n/a	43	Silt Loam	n/a	n/a	n/a	25	75	n/a	n/a	n/a	n/a	0.1	0.03
GT-116	595	9.7	0.14	n/a	54	Silt Loam	n/a	n/a	n/a	25	75	n/a	n/a	n/a	n/a	0.1	0.03
GT-19	605	9.7	0.14	0.3	n/a	n/a	1.4	0.8	9.6	n/a	n/a	72	28	0.1	0.1	0.1	n/a
GT-117	608	9.7	0.14	n/a	30	Silt Loam	n/a	n/a	n/a	23	77	n/a	n/a	n/a	n/a	0.1	0.03
GT-20	616	9.8	0.14	0.3	n/a	n/a	2.0	1.1	4.1	n/a	n/a	70	30	0.1	0.2	0.2	n/a
GT-118	620	9.8	0.14	n/a	35	Silt Loam	n/a	n/a	n/a	25	75	n/a	n/a	n/a	n/a	0.2	0.04
GT-119	688	10.3	0.14	n/a	38	Silt Loam	n/a	n/a	n/a	24	76	n/a	n/a	n/a	n/a	0.2	0.04
GT-21	698	10.4	0.14	0.3	n/a	n/a	1.8	0.9	9.6	n/a	n/a	66	34	0.1	0.2	0.2	n/a
MZW -428	709	10.5	0.14	0.3	44	Silt Loam	n/a	n/a	n/a	18	82	68	32	n/a	n/a	0.2	0.03
GT-120	716	10.5	0.14	n/a	36	Silt Loam	n/a	n/a	n/a	12	88	n/a	n/a	n/a	n/a	0.2	0.02
GT-22	726	10.6	0.14	0.4	n/a	n/a	1.5	1.0	2.7	n/a	n/a	70	30	0.04	0.2	0.2	n/a
MZW -429	742	10.7	0.14	0.3	12	Silt Loam	2.2	0.9	1.9	38	62	57	43	0.02	0.2	0.2	0.1
GT-23	751	10.8	0.14	0.2	n/a	n/a	1.5	0.6	1.5	n/a	n/a	36	64	0.01	0.1	0.2	n/a
GT-121	757	10.8	0.15	n/a	32	Silt Loam	n/a	n/a	n/a	42	58	n/a	n/a	n/a	n/a	0.2	0.1
GT-122	786	11.0	0.15	n/a	20	Silt Loam	n/a	n/a	n/a	59	41	n/a	n/a	n/a	n/a	0.1	0.1
GT-24	797	11.1	0.14	0.3	n/a	n/a	3.0	1.1	1.2	n/a	n/a	15	85	0.02	0.3	0.3	n/a
MZW -430	808	11.2	0.15	0.4	23	Silt Loam	2.7	0.9	1.8	50	50	18	82	0.03	0.3	0.3	0.2
GT-123	827	11.3	0.15	n/a	21	Silt Loam	n/a	n/a	n/a	60	40	n/a	n/a	n/a	n/a	0.3	0.2
GT-25	836	11.4	0.14	0.5	n/a	n/a	3.4	1.1	1.7	n/a	n/a	20	80	0.03	0.5	0.4	n/a
MZW -431	848	11.5	0.14	0.5	13	Silt Loam	2.8	0.9	1.7	64	36	24	76	0.04	0.5	0.5	0.3
GT-26	859	11.5	0.15	0.6	n/a	n/a	3.3	1.2	1.8	n/a	n/a	20	80	0.05	0.6	0.6	n/a
GT-124	867	11.6	0.13	n/a	24	Silt Loam	n/a	n/a	n/a	61	39	n/a	n/a	n/a	n/a	0.6	0.3
GT-27	905	11.9	0.11	0.6	n/a	n/a	3.1	1.1	3.6	n/a	n/a	18	82	0.07	0.5	0.5	n/a
MZW -432	924	12.0	0.11	0.5	22	Silt Loam	2.9	1.1	3.3	60	40	15	85	0.05	0.4	0.4	0.2
GT-28	933	12.1	0.11	0.5	n/a	n/a	3.0	1.3	3.5	n/a	n/a	20	80	0.05	0.3	0.4	n/a
GT-126	942	12.2	0.11	n/a	62	Silt Loam	n/a	n/a	n/a	45	55	n/a	n/a	n/a	n/a	0.3	0.2
GT-127	960	12.4	0.11	n/a	41	Silt Loam	n/a	n/a	n/a	30	70	n/a	n/a	n/a	n/a	0.3	0.1
GT-29	969	12.5	0.11	0.4	n/a	n/a	2.2	0.8	5.0	n/a	n/a	16	84	0.06	0.2	0.2	n/a
GT-128	977	12.5	0.11	n/a	45	Silt Loam	n/a	n/a	n/a	23	77	n/a	n/a	n/a	n/a	0.2	0.05
MZW -433	997	12.7	0.11	0.5	16	Silt Loam	2.0	0.8	4.2	38	62	13	87	0.06	0.2	0.2	0.1
GT-30	998	12.7	0.11	0.5	n/a	n/a	2.3	0.8	5.0	n/a	n/a	3	97	0.07	0.3	0.2	n/a
GT-31	1019	12.9	0.10	0.5	n/a	n/a	3.2	1.1	3.6	n/a	n/a	9	91	0.05	0.3	0.3	n/a
GT-129	1024	13.0	0.11	n/a	52	Silt Loam	n/a	n/a	n/a	48	52	n/a	n/a	n/a	n/a	0.3	0.1

Table S5. Local bedrock and soil sampling location and properties

Sample		Location	Mode	Texture	Al	Fe	Ca	>2mm	<2mm
Type	name		µm	-	[wt. %]	[wt. %]	[wt. %]	[%]	[%]
Local Bedrock	MW-05 A	Rock fragments from the well escarpment			0.10	0.04	37		
	MW-05 B				0.19	0.11	35		
	MW-06 A				0.03	0.02	36		
	MW-06 B				0.12	0.07	36		
	MW-07 A				0.08	0.04	36		
	MW-07 B				0.07	0.04	36		
	MW-09 A	Adjacent Escarpment			0.14	0.06	36		
	MW-09 B				0.11	0.07	36		
	MW-10 A				0.43	0.20	34		
	MW-10 B				0.52	0.25	34		
	MW-11 A				1.4	1.1	29		
	MW-11 B				1.5	1.1	28		
	Bedrock				1.2	0.7	33		
Soil	1-a (0-0.5 cm)		32	Silt Loam	2.2	1.1	26	9	91
	1-b (0.5-3 cm)		29	Silt Loam	3.8	2.0	18	10	90
	1-c (3-6 cm)		30	Silt Loam	2.3	1.3	27	12	88
	2-a (0-3 cm)		39	Silty Clay Loam	4.4	2.7	12	9	91
	2-b (3-8 cm)		6	Silty Clay	3.8	2.2	16	16	84
	2-c (8-12 cm)		8	Silty Clay Loam	4.1	2.3	15	9	91

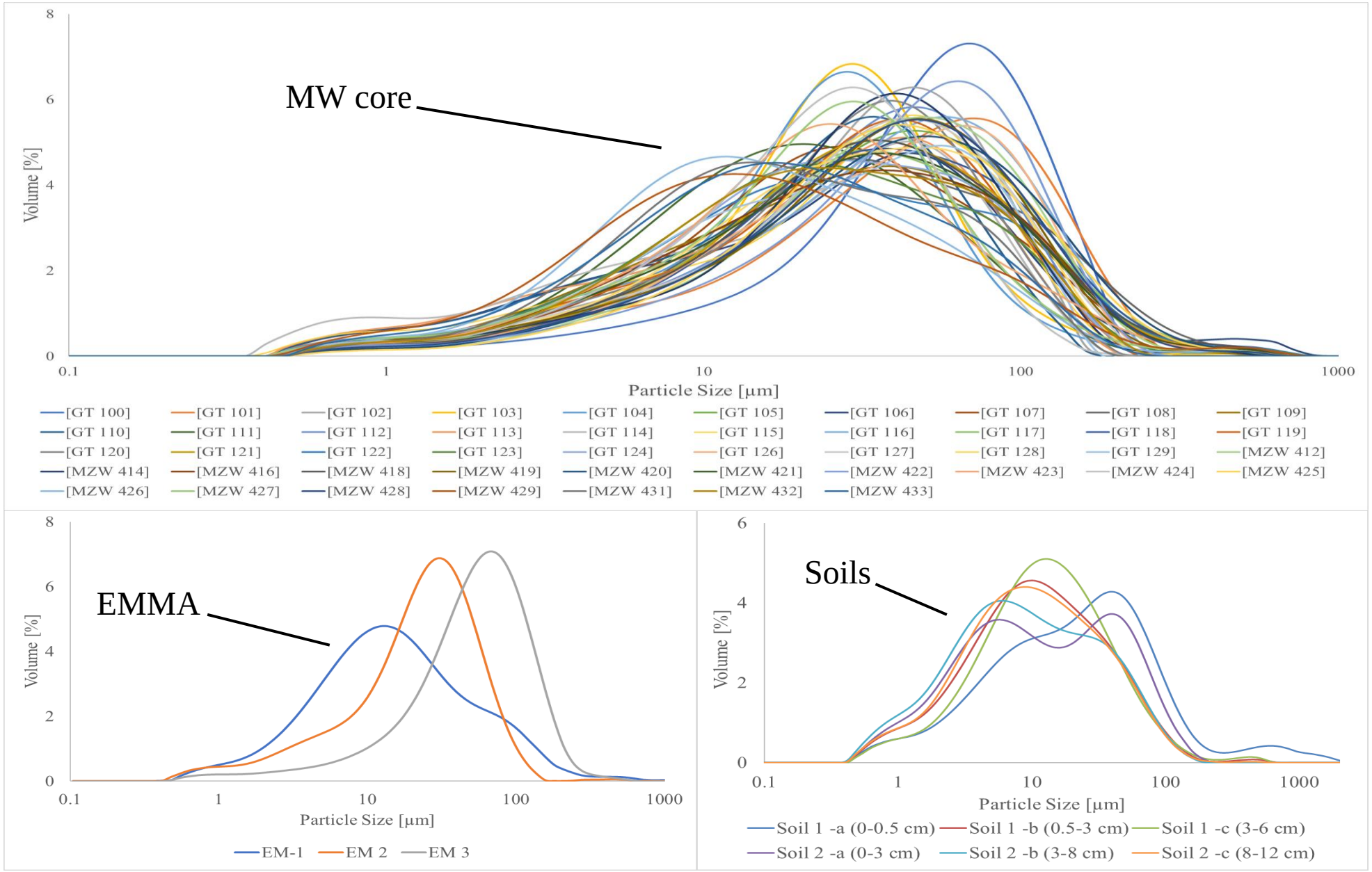

Figure S3. The MW core , EM's and adjacent soils full PSD

Table S6. Summer dust sources sampling location and properties

Sample	Geomorphic Type	Distance From MW	Mode	Texture	Vegetation	Pavement Cover	Longitude	Latitude	Al	Fe	Ca
	-	Km	μm	-	%	%	Degrees minutes seconds		[wt. %]	[wt. %]	[wt. %]
Summer -Alluvial Fan											
MB-02	Wash Bank	185	82	Sandy Loam	30	0	33° 2' 33.4" N	112° 18' 8.3" W	6.4	2.4	1.2
MB-03	Terrace Bank	185	56	Loam	0	0	33° 2' 33.4" N	112° 18' 8.3" W	6.7	2.6	1.6
MB-06	Terrace	185	68	Loam	20-40	0-20	33° 2' 24.5" N	112° 17' 48.1" W	6.4	2.3	1.3
MB-07	Terrace	185	78	Sandy Loam	20-40	0-20	33° 2' 39.6" N	112° 17' 43.7" W	6.3	2.2	1.1
CE-01	Terrace	190	74	Silt Loam	40-50	0	33° 37' 26.6" N	113° 22' 6.0" W	6.5	3.0	2.5
WL-03	Wash Bank	320	97	Sandy Loam	0	0	32° 37’ 9.9" N	114° 8' 50.2" W	6.0	2.2	2.7
WL-05	Terrace	320	105	Loam Sand	30	30	32° 37' 10.1" N	114° 7' 31.5" W			
TC-01	Terrace	300	112	Sandy Loam	5-10	20	32° 39' 49.1" N	113° 54' 18.3" W	5.6	1.7	2.1
GR-01	Wash	280	151	Loamy Sand	5	0	32° 49' 55.6" N	113° 45' 40.1" W	6.3	1.8	2.0
GR-02	Terrace	280	82	Sandy Loam	5	0	32° 49' 55.6" N	113° 45' 40.1" W	5.6	2.1	2.5
GR-03	Terrace	280	43	Silt Loam	0	0	32° 49' 57.2" N	113° 45' 36.0" W	6.2	2.5	4.7
HY-01	Wash	240	76	Loam	30	0	33° 0' 7.0" N	113° 23' 5.8" W	6.8	2.0	3.1
PD-02	Terrace	250	75	Loam	30	30	32° 34' 56.6" N	112° 52' 26.3" W	5.7	2.4	1.8
GB-02	Terrace	205	73	Loam	20-30	10	32° 57’ 54.0" N	112° 42' 9.8" W	6.8	2.8	2.1
GB-04	Terrace	205	66	Loam	20-30	30	32° 58' 12.8" N	112° 41' 20.9" W	5.5	2.8	2.9
AZ-02	Terrace	185	64	Loan	30-40	10	33° 11' 20.9" N	112° 42’ 6.0" W	5.7	2.2	2.7
CGD-01	Agriculture Field	180	51	Loam	n/a	n/a	33° 7' 14.1" N	112° 0' 31.1" W	6.0	2.4	1.2
CGD-02	Agriculture Field	180	43	Silt Loam	n/a	n/a	32° 46' 41.5" N	111° 37' 49.8" W	n/a	n/a	n/a
CGD-03	Agriculture Field	180	76	Loam	n/a	n/a	32° 46' 13.3" N	111° 23' 1.0" W	n/a	n/a	n/a
CGD-04	Agriculture Field	180	57	Loam	n/a	n/a	32° 40' 48.6" N	111° 28' 19.6" W	n/a	n/a	n/a
Summer –Wash											
UT-03	Fine and wide wash	225	55	Silt Loam	0-20	0	33° 48' 7.8" N	113° 55' 29.2" W	6.7	3.0	3.0
UT-04	Fine and wide wash adjacent to vegetation	225	65	Loam	20-30	0	33° 48' 8.6" N	113° 55' 28.7" W	6.5	2.6	3.2
UT-05	Fine and wide wash	225	20	Silty Clay Loam	0-20	0	33° 48' 12.4" N	113° 55' 31.1" W	7.4	3.3	3.7
NH-01	Fine and wide wash	220	41	Silt Loam	0-20	10-30	33° 37’ 8.9" N	113° 46' 35.9" W	6.6	2.9	4.4
NH-02	Fine and wide wash	220	51	Silt Loam	0-20	10-30	33° 37' 7.2" N	113° 46' 40.7" W	6.1	2.7	3.9
CE-03	Fine and wide wash	190	7	Silty Clay Loam	0-20	0	33° 36' 59.3" N	113° 25' 33.7" W	7.9	3.7	3.0
CE-04	Fine and wide wash adjacent to vegetation	190	9	Silty Clay Loam	20-30	0	33° 36' 59.3" N	113° 25' 33.7" W	n/a	n/a	n/a
Summer -Flood Plain											
PL-01	Gila flood plain	250	74	Loam	10-20	0	32° 54’ 36.0" N	113° 32' 31.9" W	5.9	2.4	3.1
PL-02	Gila flood plain	250	85	Sandy Loam	10-20	0	32° 54’ 36.0" N	113° 32' 31.9" W	5.8	2.1	2.7
PL-04	Gila flood plain	250	27	Silt Loam	10-20	0	32° 51' 45.2" N	113° 32' 31.1" W	6.7	3.5	5.1
GB-03	Flood plain adjacent to current stream	205	53	Silt Loam	10-30	0	32° 59' 39.7" N	112° 42' 48.1" W	7.0	3.6	4.2
GR-04	Agriculture Gila flood plain	280	68	Sandy Clay	0	0	32° 50' 23.4" N	113° 43’ 49.4" W	5.6	1.8	2.0

Table S7. Winter dust sources sampling location and properties

Sample	Geomorphic Type	Distance From MW	Mode	Texture	Vegetation	Pavement Cover	Longitude	Latitude	Al	Fe	Ca
	-	Km	µm	-	%	%	Degrees minutes seconds		[wt. %]	[wt. %]	[wt. %]
Winter-Playa											
KG-01	Playa	245	n/a	n/a	0	0	35° 40' 19.0" N	114° 6' 43.6" W	7.1	4.2	5.8
KG-02	Playa	245	3	Silty Clay	0	0	35° 40’ 18.0" N	114° 6' 38.4" W	7.1	3.9	5.5
KG-03	Playa Sample adjacent to vegetation	245	16	Silty Clay	30	0	35° 40' 24.4" N	114° 6’ 36.0" W	6.6	3.7	6.5
KG-04	Wash	230	11	Silty Clay Loam	0-30	0	35° 34' 54.5" N	114° 3' 5.1" W	7.2	4.0	3.5
KG-05	Wash adjacent to vegetation	230	6	Silty Clay Loam	0-30	0	35° 34' 54.5" N	114° 3' 5.1" W	n/a	n/a	n/a
KG-06	Terrace	230	43	Silt Loam	10-30	10-20	35° 34’ 30.0" N	114° 3' 35.2" W	n/a	n/a	n/a
KG-07	Terrace	230	n/a	n/a	10-30	10-20	35° 34’ 30.0" N	114° 3' 35.2" W	3.8	1.7	7.3
Winter-Flood Plain											
BH-07	Colorado River Flood Plain	270	43	Silt Loam	10-20	0	35° 0’ 53.0" N	114° 38' 55.9" W	4.0	1.5	4.6
BH-08	Colorado River Flood Plain	270	6	Clay Loam	10-20	0	34° 58' 58.8" N	114° 39' 54.9" W	7.6	3.2	5.1

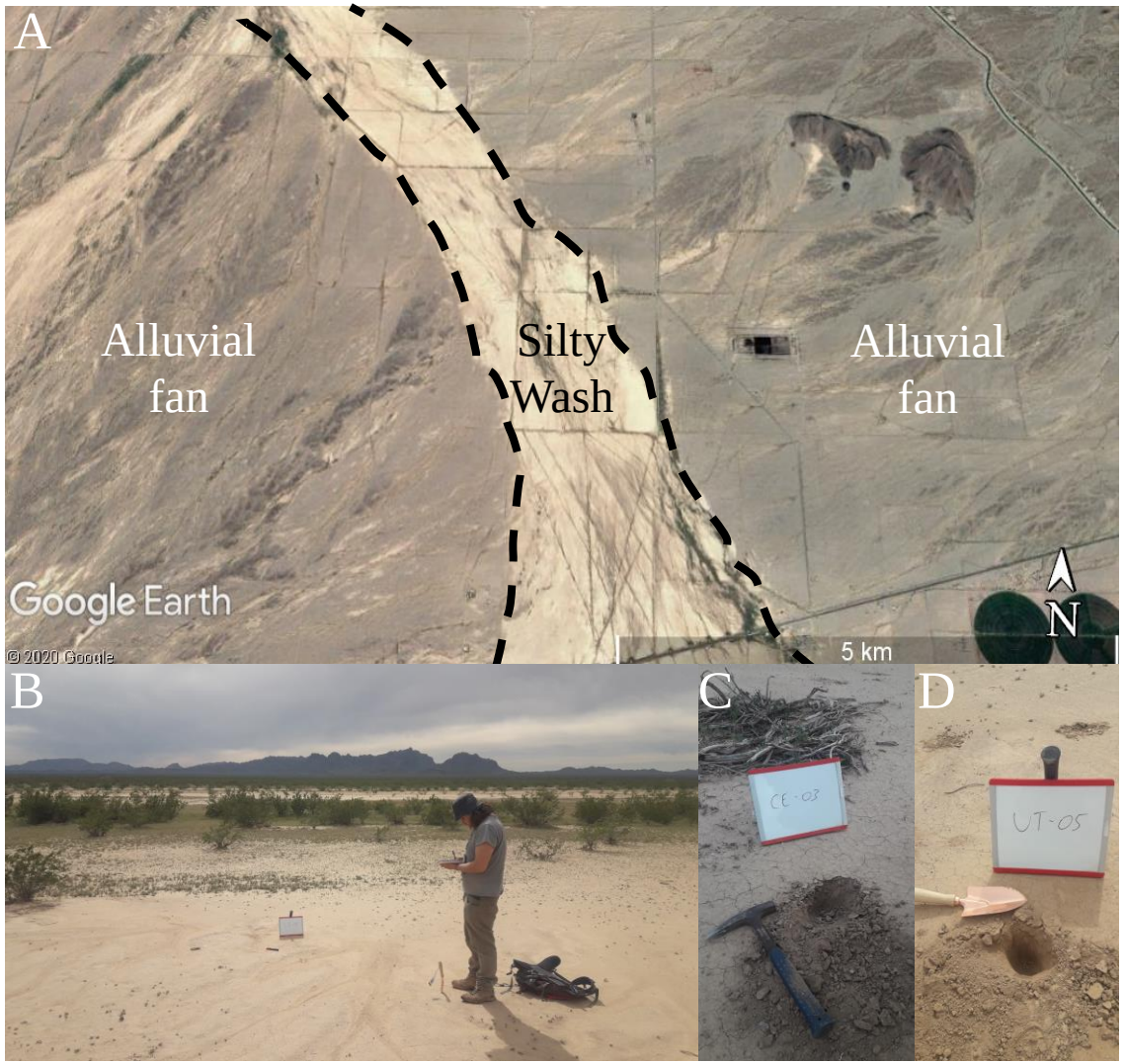

Figure S4. A. Aerial photo (via Google Earth) of Utting wash (UT) and adjacent alluvial fans; B. Field photo of Utting wash, note the limited coverage of gravels and vegetation; C. and D. A 5 cm pit at Utting (UT) and Centennial (CE) washes revealing silt loam to silty clay loam sediments.

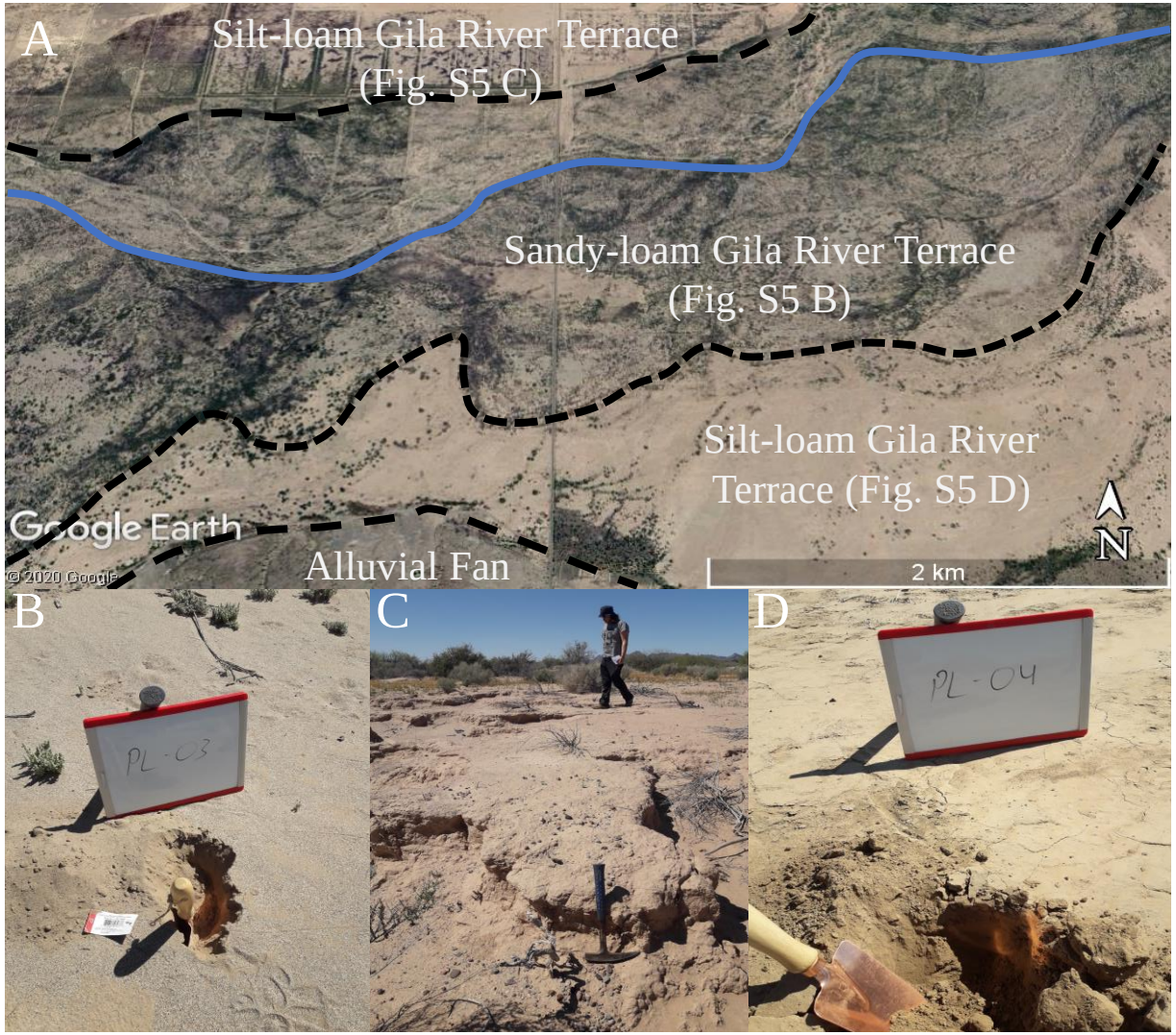

Figure S5. A. Aerial photo (via Google Earth) of Gila River flood plains. Gila River is marked in blue, the active, lower floodplains are adjacent to the river, whereas two elevated terraces appear farther away from the active floodplains; B. A 5 cm pit at the lower floodplain reveals coarse sand sediments; C. and D. The elevated terraces exhibit loam texture sediments and bare surfaces, mostly free of gravel.

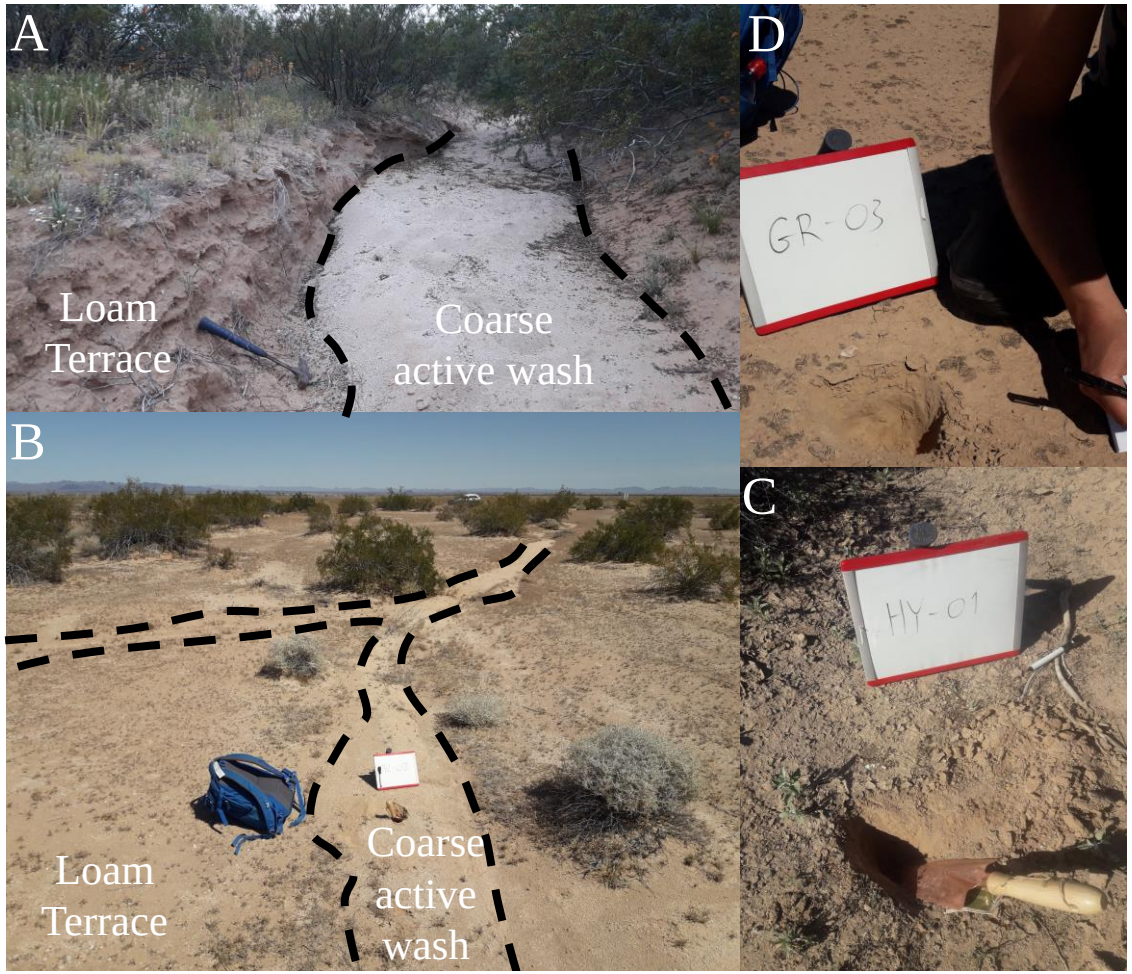

Figure S6. Field photos of alluvial fans: A. Mobile alluvial fan (MB) composed of loam textured terraces incised by 3 m wide active washes, rich with sand; B. Tacna alluvial fan (TC) composed of bare loam textured terraces incised by 2 m wide active washes, rich with sand; C. Terrace at Hyder (HY) alluvial fan, characterized by loam textured sediments and low coverage of vegetation and gravels; D. Terrace at Growler (GR) alluvial fan characterized by bare surface and silt loam textured sediments.

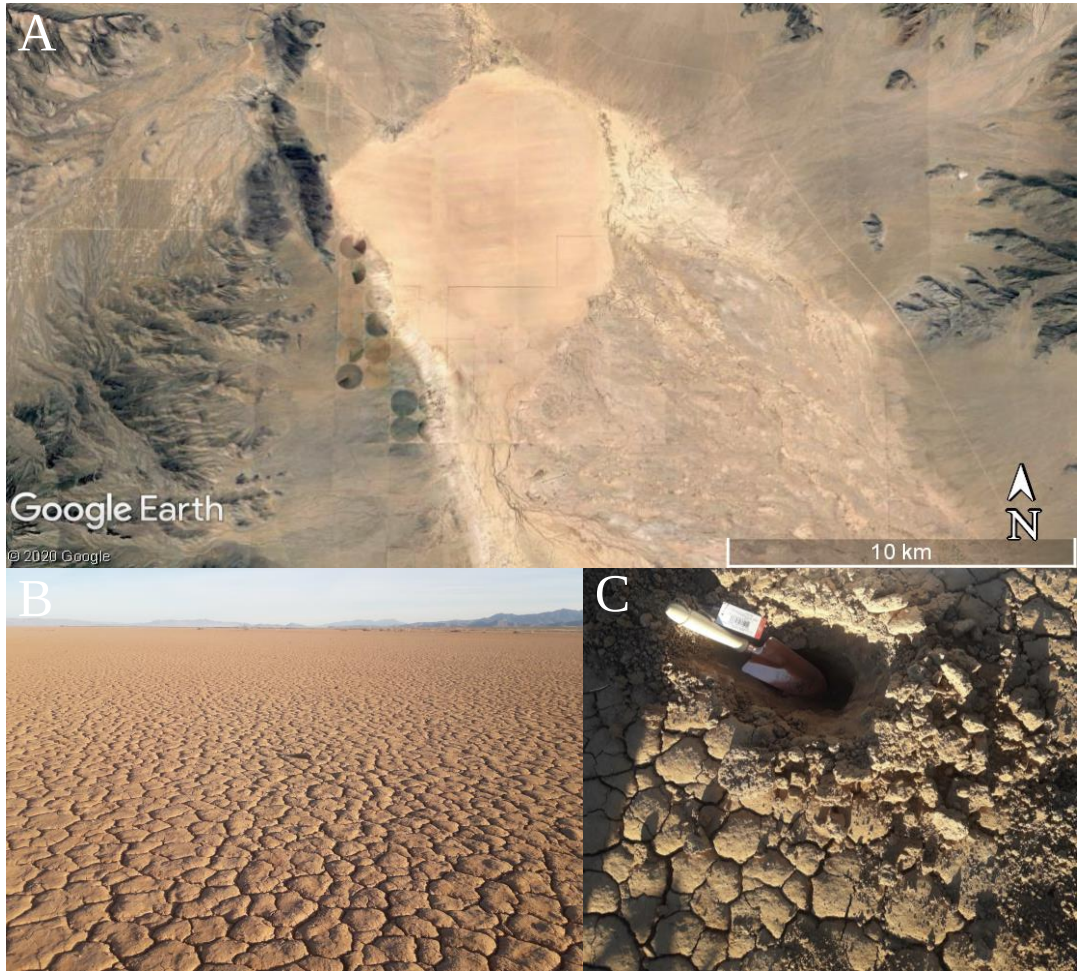

Figure S7. A. Aerial photo (via Google Earth) of Kingman playa (KG). Note that an active wash drains the plays to the south; B. and C. Field photos of the playa bare surface, showing a well-developed physical crust (mud polygons), the sediments beneath the crust are of silty clay texture.

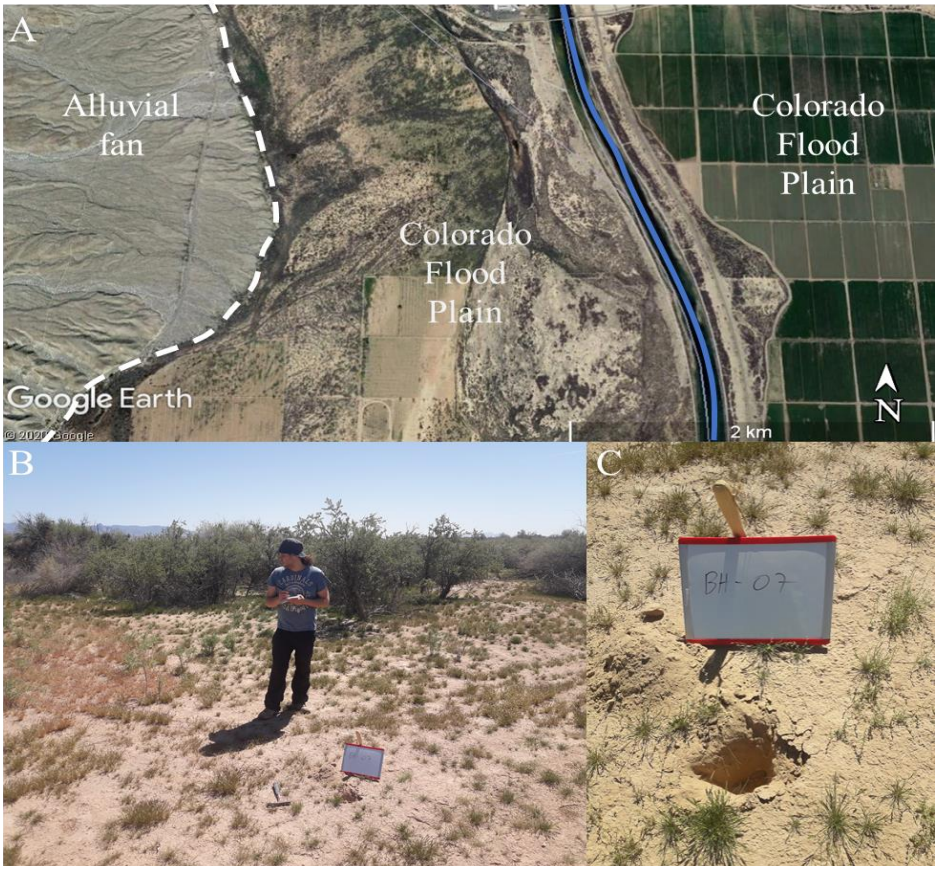

Figure S8. A. Aerial photo (via Google Earth) of Colorado River flood plains currently used for agriculture, and the current Colorado River (blue). B. and C. Field photos of the flood plains covered with annual vegetation, weak crust, and silt loam textured sediments.

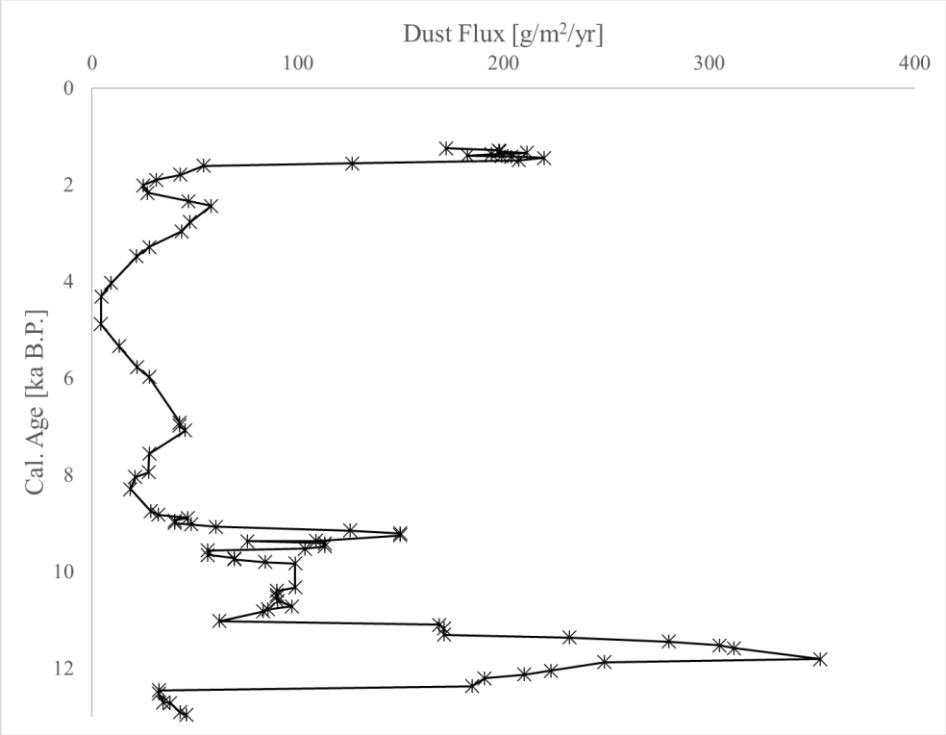

Figure S9. Moving average of total dust flux calculated according to equation 3, with Al values divided by the average UCC value instead of the average local bedrock value.

References

Arcusa, S.H., Mckay, N.P., Routson, C.C., and Munoz, S.E., 2019, Dust-drought interactions over the last 15 , 000 years : A network of lake sediment records from the San Juan Mountains , Colorado: The Holocene, doi:10.1177/0959683619875192.

Baddock, M.C., Ginoux, P., Bullard, J.E., and Gill, T.E., 2016, Do MODIS-defined dust sources have a geomorphological signature? Geophysical Research Letters, v. 43, p. 2606–2613, doi:10.1002/2015GL067327.

Blaauw, M., and Christeny, J.A., 2011, Flexible paleoclimate age-depth models using an autoregressive gamma process: Bayesian Analysis, v. 6, p. 457–474, doi:10.1214/11-BA618.

Breed, C., and Reheis, M., 1999, Desert Winds : Monitoring Wind-Related Surface Processes in Arizona , New Mexico , and California: U.S. Geological Survey Professional Paper 1598, p. 158, http://dl.dropbox.com/u/1674920/Salinity/p1598so.pdf.

Brenner, I.B., Watson, A.E., Russell, G.M., and Goncalves, M., 1980, A new approach to the determination of the major and minor constituents in silicate and phosphate rocks: Chemical Geology, v. 28, p. 321–330.

Crouvi, O., Amit, R., Enzel, Y., Porat, N., and Sandler, A., 2008, Sand dunes as a major proximal dust source for late Pleistocene loess in the Negev Desert, Israel: Quaternary Research, v. 70, p. 275–282, doi:10.1016/j.yqres.2008.04.011.

Davis, O.K., and Shafer, D.S., 1992, A Holocene climatic record for the Sonoran Desert from pollen analysis of Montezuma Well, Arizona, USA: Palaeogeography, Palaeoclimatology, Palaeoecology, v. 92, p. 107–119, doi:10.1016/0031-0182(92)90137-T.

Dietze, E., Hartmann, K., Diekmann, B., IJmker, J., Lehmkuhl, F., Opitz, S., Stauch, G., Wünnemann, B., and Borchers, A., 2012, An end-member algorithm for deciphering modern detrital processes from lake sediments of Lake Donggi Cona, NE Tibetan Plateau, China: Sedimentary Geology, v. 243–244, p. 169–180, doi:10.1016/j.sedgeo.2011.09.014.

Draxler, R.R., and Hess, G.D., 1998, An overview of the HYSPLIT-4 modelling system for trajectories, dispersion and deposition: Australian Meteorological Magazine, v. 47, p. 295– 308.

Ginoux, P., Garbuzov, D., and Hsu, N.C., 2010, Identification of anthropogenic and natural dust sources using moderate resolution imaging spectroradiometer (MODIS) deep blue level 2 data: Journal of Geophysical Research Atmospheres, v. 115, p. 1–10, doi:10.1029/2009JD012398.

Longman, J., Veres, D., Ersek, V., Salzmann, U., Hubay, K., Bormann, M., Wennrich, V., and Schäbitz, F., 2017, Periodic input of dust over the Eastern Carpathians during the Holocene linked with Saharan desertification and human impact: Climate of the Past, v. 13, p. 897–917, doi:10.5194/cp-13-897-2017.

Paterson, G.A., and Heslop, D., 2015, New methods for unmixing sediment grain size data: Geochemistry, Geophysics, Geosystemseosystems, p. 4494–4506, doi:10.1002/2015GC006070.

Pratte, S., Garneau, M., and De Vleeschouwer, F., 2017, Increased atmospheric dust deposition during the Neoglacial in a boreal peat bog from north-eastern Canada: Palaeogeography, Palaeoclimatology, Palaeoecology, v. 469, p. 34–46, doi:10.1016/j.palaeo.2016.12.036.

Reimer, P.J., Edouard Bard, B., Alex Bayliss, B., Warren Beck, B.J., Paul Blackwell, B.G., and Christopher Bronk Ramsey, B., 2013, Intcal13 and Marine13 Radiocarbon Age Calibration Curves 0–50,000 Years Cal Bp: Radiocarbon, v. 55, p. 1869–1887, doi:10.1017/S0033822200048864.

Weltje, G.J., 1997, End-member modeling of compositional data: Numerical-statistical algorithms for solving the explicit mixing problem: Mathematical Geology, v. 29, p. 503–549, doi:10.1007/bf02775085.

Weltje, G.J., and Prins, M.A., 2003, Muddled or mixed? Inferring palaeoclimate from size distributions of deep-sea clastics: Sedimentary Geology, v. 162, p. 39–62, doi:10.1016/S0037-0738(03)00235-5.

Yu, Z., Robinson, P., and McGoldrick, P., 2001, An evaluation of methods for the chemical decomposition of geological materials for trace element determination using ICP-MS: Geostandards Newsletter, v. 25, p. 199–217, doi:10.1111/j.1751-908x.2001.tb00596.x.